Research Article | Vol. 14, No. 11 / 1 Nov 2023 / Biomedical Optics Express 5764

Biomedical Optics EXPRESS

Multimodal imaging of metabolic activities for distinguishing subtypes of breast cancer

ZHI LI,[1] CHLOE NGUYEN,[1] HONGJE JANG,[1] DAVID HOANG,[1] SOESU MIN,[2] ELLEN ACKERSTAFF,[2] JASON A. KOUTCHER,[2,3,4] AND LINGYAN SHI[1,*]

[1] Department of Bioengineering, University of California San Diego, California, USA
[2] Department of Medical Physics, Memorial Sloan Kettering Cancer Center, New York, USA
[3] Department of Medicine, Memorial Sloan Kettering Cancer Center, New York, USA
[4] Weill Cornell Medical College, Cornell University, New York, USA
[*] l2shi@ucsd.edu

Abstract: Triple negative breast cancer (TNBC) is a highly aggressive form of cancer. Detecting TNBC early is crucial for improving disease prognosis and optimizing treatment. Unfortunately, conventional imaging techniques fall short in providing a comprehensive differentiation of TNBC subtypes due to their limited sensitivity and inability to capture subcellular details. In this study, we present a multimodal imaging platform that integrates heavy water (D_2O)-probed stimulated Raman scattering (DO-SRS), two-photon fluorescence (TPF), and second harmonic generation (SHG) imaging. This platform allows us to directly visualize and quantify the metabolic activities of TNBC subtypes at a subcellular level. By utilizing DO-SRS imaging, we were able to identify distinct levels of de novo lipogenesis, protein synthesis, cytochrome c metabolic heterogeneity, and lipid unsaturation rates in various TNBC subtype tissues. Simultaneously, TPF imaging provided spatial distribution mapping of NAD[P]H and flavin signals in TNBC tissues, revealing a high redox ratio and significant lipid turnover rate in TNBC BL2 (HCC1806) samples. Furthermore, SHG imaging enabled us to observe diverse orientations of collagen fibers in TNBC tissues, with higher anisotropy at the tissue boundary compared to the center. Our multimodal imaging platform offers a highly sensitive and subcellular approach to characterizing not only TNBC, but also other tissue subtypes and cancers.

© 2023 Optica Publishing Group under the terms of the Optica Open Access Publishing Agreement

1. Introduction

Breast cancer is the most prevalent non-skin cancer among women in the United States, and it encompasses various molecular subtypes [1]. Among these subtypes, triple negative breast cancer (TNBC) stands out as an aggressive form of the disease, characterized by a poor prognosis and a high incidence of metastasis to the brain, lung, and liver [2]. TNBC is distinguished by its "basal-like" molecular profile, aggressive behavior, distinct metastatic patterns, and absence of successful targeted therapy. Its name originates from the absence of clinically detectable expression of estrogen and progesterone receptors (ER/PR), as well as the hormone epidermal growth factor receptor (HER2) protein [3]. Molecular profiling has further classified TNBC into six categories: basal-like 1 (BL1), basal-like 2 (BL2), immunomodulatory (IM), mesenchymal-like (M), mesenchymal stem-like (MSL), and luminal androgen-receptor (LAR) expressing subtypes. Each of these TNBC subtypes demonstrates varying responses to chemotherapy and targeted treatment approaches [4].

The early detection of TNBC plays a vital role in enhancing disease prognosis and treatment outcomes. TNBC is typically diagnosed with a procedure of imaging and immunohistochemistry [5]. Various imaging modalities including mammography, ultrasound, magnetic resonance imaging (MRI), positron emission tomography (PET), and computed tomography (CT) have been employed for TNBC detection [6]. However, these approaches often lack the required specificity

#500252 https://doi.org/10.1364/BOE.500252
Journal © 2023 Received 11 Jul 2023; revised 25 Sep 2023; accepted 25 Sep 2023; published 13 Oct 2023

Biomedical Optics EXPRESS

and fail to provide temporal and spatial information at the subcellular level for accurate subtyping of TNBC. Consequently, misdiagnosis, ineffective treatment, and tumor metastasis can occur. To address these limitations, Raman scattering spectroscopy/microscopy has emerged as a promising method for early TNBC diagnosis and subtype discrimination [7,8]. By detecting the vibrations of chemical bonds within molecules, such as CH_2 in lipid and CH_3 in protein [9–11], Raman scattering technique offers precise information about the content and composition of various biomolecules in cells with exceptional chemical selectivity. Stimulated Raman scattering (SRS) microscopy, as an advanced imaging technology, exhibits high signal intensity and chemical sensitivity. Through the incorporation of different probes, SRS enables the visualization of metabolic dynamics of biomolecules such as lipids, proteins, and DNA in living cells and organisms, providing in situ characterization [12–15]. SRS based metabolic imaging concept has been applied to reveal diet-regulated and aging driven metabolic alterations [16–19].

In this study, we developed a multimodal imaging system that combines heavy water (D_2O)-probed SRS (DO-SRS), two-photon fluorescence (TPF), and second harmonic generation (SHG) imaging for TNBC subtyping. Our primary objective was to differentiate TNBC subtypes based on various characteristics, including lipid and protein metabolism, optical oxidation-reduction (redox) state, and the morphology of collagen fibers. Of note, dysregulation of lipid and protein metabolism are hallmarks associated with TNBC [7]. Redox metabolism, which plays a vital role in cellular metabolism, undergoes disruption in cancer [20]. Additionally, the organization of collagen fibers has been linked to breast cancer prognosis [21]. DO-SRS allows us to differentiate lipid and protein metabolic dynamics in different tumor tissues. TPF and SHG imaging enable us to evaluate the oxidation-reduction (redox) ratio by measuring nicotinamide adenine dinucleotide (NADH) and flavin adenine dinucleotide (FAD) levels, and to characterize collagen fibers in tissues, respectively.

2. Materials and methods

2.1. Cells and cell culture

All human cell lines (Table S1) were obtained from ATCC and cultured in Dulbecco's Modified Eagle's Medium (DMEM, Corning Cat. No. 10-017 or Thermo Fisher Scientific Cat. No. 12100) supplemented with 10% fetal calf serum plus 100 U/ml Penicillin and 100 µg/ml Streptomycin in a humidified incubator at 37°C in 5% CO_2 in air (resulting in 20% oxygen), as described previously [22]. The culture medium, phosphate-buffered saline without calcium or magnesium (PBS), Hanks balanced salt solution without calcium or magnesium (HBSSnoCaMg) and 0.25% Trypsin/0.25% EDTA were prepared by the Media Preparation Facility (Memorial Sloan Kettering Cancer Center, New York, NY).

2.2. Cell doubling time

For cell doubling time experiments, 7×10^4 HCC1806, 9×10^4 HCC70, 9×10^4 MDA-MB-468, 5×10^4 MDA-MB-231, and 6×10^4 BT-474 cells were seeded in 1 ml per well in 24-well plates (Corning 3524 or BD Falcon 353047 or such) and allowed to attach for 24 h &HCC1806, MDA-MB-468 and BT-474) or 48 h (MDA-MB-231 and HCC70), respectively. After attachment of cells, all wells containing cells were imaged daily with the direct cell counting protocol on a Celigo Image Cytometer (Nexcelom Bioscience, Lawrence, MA). The cell culture medium was replaced daily. After optimizing the direct cell counting analysis parameter settings, as per manufacturer's instructions, total cell counts were obtained daily for each well and cell line from the images. Cell doubling times were calculated based on exponential cell growth using GraphPad Prism v9.3.1 (64-bit Windows10, GraphPad Software, LLC, San Diego, CA 9210).

Biomedical Optics EXPRESS

2.3. In vivo tumor xenograft studies

For tumor cell injection, cells were expanded in single (Sarstedt, Germany) and multi-layer (3 or 5, Corning™ Falcon™ Cell Culture Multi Flasks) and harvested at ~70-90% confluence by trypsination (0.25% Trypsin/0.25% EDTA in HBSSnoCaMg or PBS), following removal of culture medium and 1x wash with PBS. After spinning down the cells into a pellet to remove the by culture-medium inactivated trypsin, the cells were washed once in PBS before the cells were pelleted and transferred on ice to the Antitumor Assessment Core at MSK for tumor implantation. All *in vivo* tumor xenograft studies at MSKCC were performed in accordance with procedures in an approved IACUC protocol.

To establish human tumor xenografts, 5×10^6 cells HCC70 (AA), 1×10^7 cells HCC1806 (AA), 1×10^7 cells MDA-MB-486 (AA), 1×10^7 cells MDA-MB-231 (Cauc), and 1×10^7 cells BT-474 (Cauc, Non-TNBC control) were co-injected with Matrigel (Corning Cat. No. 356237, Lot No. 0248001; 1:1 volume mix, total of 150 µl injected) into the 4th mammary fat pad of 32 days (4.6 weeks) old, female athymic nude mice (outbred, Stock 69, derived from nucleus colony obtained from the National Cancer Institute, Frederick, MD; Envigo, US) via surgical mammary fat pad injection performed by the Antitumor Assessment Core at MSKCC. One day prior to the tumor cell implantation, the mice standard chow (PicoLab Rodent Diet 20, Cat. No. 5053, LabDiet, St. Louis, MO) was exchanged for high-fat chow containing amoxicillin (LabDiet 5058 w/ 0.12% Amoxicillin, Cat. No. 5BQ1, LabDiet, St. Louis, MO) to prevent opportunistic infections by rodent pathogens, such as Corynebacterium bovis, and thus, preventing scaly dermatitis [23].

Once tumors were established, the tumor size was measured thrice weekly by sliding-jaw caliper, as described previously [24]. Tumor volumes were calculated from three orthogonal tumor diameters (length l, width w and height h) of the tumor by ellipsoid formula $\pi/6$ x l x w x h[24]. Once tumors reached ~ 100-110 mm^3 for MDA-MB-468, MDA-MB-231, HCC70, BT-474, and ~ 260 mm^3 for HCC1806 by caliper measurement, the acidified drinking water was exchanged for acidified drinking water containing 25% heavy water (Deuterium Oxide, Cat. No. DLM-2259, 99.87% D, Lot No. PR-31618, microbiological tested, Cambridge Isotope Laboratories, Inc., Andover, MA) and supplied ad libitum for (7.904 ± 0.036) days (mean ± SD). This leads to accumulation of deuterated metabolites in tissues, enhancing Raman Spectroscopy studies. After 8 days, tumors were excised and fixed for (93.1 ± 2.1) h (mean ± SD) in 10% buffered Formalin (Cat. No. SF100-4, Fisher Scientific, part of Thermo Fisher Scientific) at 4 °C, after which the tumor tissues were stored in 1x PBS w/o Ca^{2+} & Mg^{2+} at 4 °C until overnight shipment with cold packs to San Diego for *ex vivo* Raman studies. At time of excision, the fast-growing and larger HCC1806 tumors tended to be squashy and liquid, that is necrotic, in the center. For the slower-growing BT-474, mice were exposed for 12 days to acidified drinking water containing 25% heavy water before tumor excision.

Tumor doubling times were calculated based on exponential tumor growth using GraphPad Prism v9.3.1 (64-bit Windows10, GraphPad Software, LLC, San Diego, CA). For both, cell and tumor doubling times, the data were linearized and fitted to a straight line to obtain doubling times and corresponding standard error.

2.4. Spontaneous Raman spectroscopy

Raman spectra of all the tissue samples were measured by a Raman spectrometer connected to a confocal Raman microscope (XploRA PLUS, Horiba). A 532 nm diode line focus laser (~40 mW at the sample) was focused on the cells with the help of a 100x objective (MPLN100X, Olympus). The laser power on the sample was optimized to avoid any damage to the cells. A cooled charge coupled device (CCD) detector fitted to a 2400 grooves/mm grating spectrometer was used to detect the signal. Spectra were collected at 40 s acquisitions with an accumulation of 3. The background spectra were taken for each tissue point at the same focus plane and were subtracted from original spectrum immediately. Spectra were preprocessed using vector normalization and

Biomedical Optics EXPRESS

simplex normalized. The instrumental calibration was verified using the silicon line at 520 cm^{-1}. The observed data were processed and analyzed using custom codes written in Python.

2.5. Multimodal imaging system

An upright laser-scanning microscope (DIY multiphoton, Olympus) with a 25x water objective (XLPLN, WMP2, 1.05 NA, Olympus) was applied for near-IR throughput. Synchronized pulsed pump beam (tunable 780–990 nm wavelength, 5–6 ps pulse width, and 80 MHz repetition rate) and Stokes beam (wavelength at 1031 nm, 6 ps pulse width, and 80 MHz repetition rate) were supplied by a picoEmerald system (Applied Physics & Electronics) and coupled into the microscope. The pump and Stokes beams were collected in transmission by a high NA oil condenser (1.4 NA). In two photon fluorescence (TPF) mode, 780 nm and 860 nm pump laser were used to excite NADH and FAD molecules, respectively. All images obtained were 512×512 pixels, with a dwell time of 8 µs. In SHG imaging mode, only the 1031 nm Stokes laser was used. All images obtained were 512×512 pixels, with a dwell time of 8 µs. In DO-SRS mode, The Stokes beam and a tunable pump laser were used. A high O.D. shortpass filter (950 nm, Thorlabs) was used that would completely block the Stokes beam and transmit the pump beam only onto a Si photodiode for detecting the stimulated Raman loss signal. The output current from the photodiode was terminated, filtered, and demodulated by a lock-in amplifier at 20 MHz. The demodulated signal was fed into the FV3000 software module FV-OSR (Olympus) to form image during laser scanning. All images obtained were 512×512 pixels, with a dwell time of 80 µs. A background image was acquired at 1900cm^{-1} and subtracted from all SRS images using Fiji (ImageJ).

2.6. Statistical analysis

For the purpose of clustering, the Spontaneous Raman spectra were analyzed, comprising of 10 spectra from 5 tumors per subtype. Specifically, 2 spectra were acquired from each tumor per subtype. Spectral clustering was processed with t-SNE to reduce the dimensionality followed with k-means unsupervised clustering algorithm in Python 3.9. Images were processed using ImageJ and Python to conduct denoising and smooth. All of images utilized for statistical analysis consist of 7 or 8 ROIs from 5 tumors per subtype, approximately 1 or 2 ROIs from each tumor per subtype. One-way ANOVA test was performed for statistical analysis.

3. Results and discussion

3.1. Multimodal imaging platform

Figure 1(A) illustrates the setup of the multimodal imaging platform. By tuning the lasers and modifying the filters, multimodal imaging can be achieved. For SRS imaging, a tunable laser (780–990 nm) is used as the pump beam and a 1031 nm beam as the Stokes beam, respectively. D_2O probing is further integrated with SRS for metabolic imaging. The deuterium (D) from D_2O is metabolized into newly synthesized biomolecules, such as lipids and proteins, to form C-D bonds. By using SRS microscopy to track the C-D bonds, the spatiotemporal metabolic processes can be visualized in organisms in situ. In TPF imaging mode, laser beams at 780 nm and 860 nm are used to excite NADH and FAD, respectively. In SHG imaging mode, the 1031 nm beam is used for examining collagen fiber morphology.

Breast cancer tissues were collected from mouse xenograft derived from TNBC cell lines from different subtypes, including HCC70 (BL2), HCC1806 (BL2), MDA-MB-468 (BL1) and MDA-MB-231 (MSL), as well as non-TNBC cells (BT-474), as summarized in Fig. 1(B). Three cell lines were of African American (AA) origin and were characterized as BL1 or BL2, while the MSL and the non-TNBC control cell lines were of Caucasian (Cauc) origin. The cell and tumor doubling times (DTs) for the 5 cell lines are summarized in Table S1 (Supplement 1).

Biomedical Optics EXPRESS

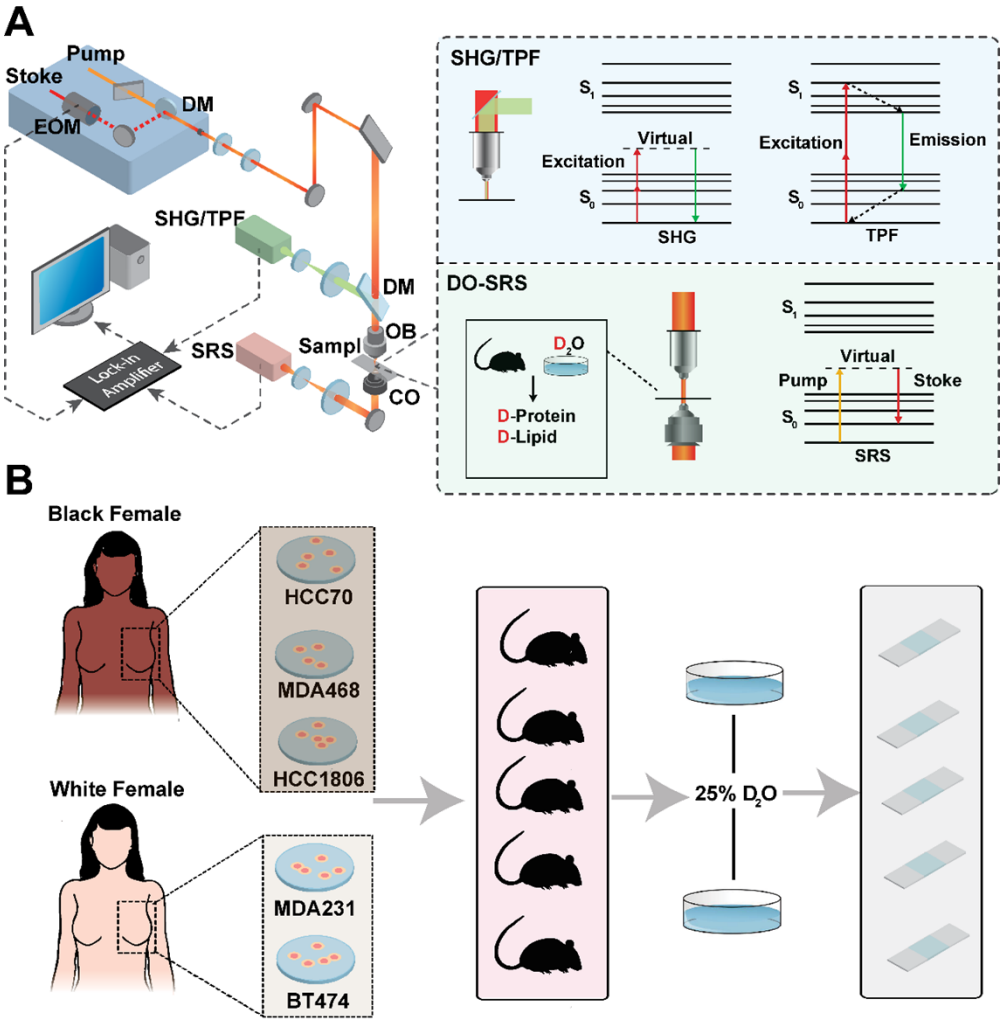

Fig. 1. Multimodal imaging platform of DO-SRS, TPF, and SHG for subtyping TNBC. (A) Schematic diagram of the multimodal imaging platform. In DO-SRS mode, a 1031 nm laser is used as the Stokes beam, and the pump laser beam is tuned to different wavelength to acquire images of different molecules. In TPF mode, the 791 nm pump laser is used to image flavin and NADH in tissues. In SHG mode, the 1031 nm Stokes laser is used to image collagen fiber in tissue. (B) TNBC tissue samples were harvested from xenograft mouse model. Different subtypes of human TNBC cell lines were xenografted in mouse, including HCC70 (BL2), HCC1806 (BL2), MDA-MB-468 (BL1) and MDA-MB-231 (MSL). Non-TNBC cells (BT-474) were used as control. For each subtype, 5 slices were sectioned from 5 different tumor tissues.

Biomedical Optics EXPRESS

3.2. DO-SRS imaging characterizing lipids and protein metabolic activity in TNBC tissues

Initially, we obtained Raman spectra of the extracellular matrix (ECM) from tissue samples using spontaneous Raman spectroscopy (Figure S2). The obtained spectra were analyzed, and the relevant Raman peaks were identified and assigned in Table S2 [25]. The averaged and normalized spectra of each TNBC subtype were compared, with normalization done relatively to the highest peak intensity at 2930 cm^{-1}, corresponding to the C-H stretch of protein (Fig. 2(A)). Multiple peaks were detected in the C-D region (2000 - 2400 cm^{-1}) and C-H stretching region (2800 - 3150 cm^{-1}), which are corresponding to newly synthesized and existing biomolecules, respectively. Notably, the TNBC subtypes exhibited different spectral intensities and shapes at these peaks, suggesting variations in protein metabolism among the subtypes (Fig. 2(A), magnified figures). The subtype BL2 (HCC1806) displayed the highest intensity at the 2186 cm^{-1} peak associated with newly-synthesized protein, while the non-TNBC tissue (BT-474) had the lowest intensity, indicating elevated protein metabolism in TNBC tissues compared to non-TNBC tissue. As these spectra were collected from the ECM, the observed spectral differences may indicate distinct microenvironments across the TNBC subtypes. To further differentiate the spectra of each TNBC subtype, we employed a method called k-means clustering algorithm, preceded by dimensionality reduction using t-distributed stochastic neighbor embedding (t-SNE) [26]. By analyzing 10 spectra from the ECM of each subtype, we assessed the classification capability of t-SNE-k-means clustering for TNBC subtyping. The clustering process successfully categorized the spectra into five distinct groups, as demonstrated in Fig. 2(B).

To explore the spatial variations in metabolism among different tumor subtypes, we employed our multimodal imaging system to analyze distinct biomolecules within the same region of interest (ROI) in each tissue sample. Initially, we utilized the two-photon fluorescence (TPF) modality to image flavin adenine dinucleotide (FAD) and nicotinamide adenine dinucleotide (NADH). Subsequently, we employed second harmonic generation (SHG) imaging to visualize collagen fibers, and further investigated lipid and protein metabolism using DO-SRS, generating stimulated Raman histology (SRH) images (Fig. 2(D)-(H)). We hypothesized that de novo protein synthesis and lipogenesis could serve as indicators for differentiating TNBC subtypes. To test this hypothesis, we acquired SRS images targeting newly-synthesized lipid and protein (CD_L and CD_P) at 2130 and 2180 cm^{-1}, as well as total lipid and protein (CH_L and CH_P) at 2850 and 2930 cm^{-1}, respectively (Figure S3). By calculating the ratiometric images of CD_P/CD_L, we were able to assess the metabolic rates in different TNBC subtypes. Notably, the HCC1806 tissue (subtype BL2) exhibited the highest protein metabolism among all TNBC tissues, while all TNBC tissues displayed higher CD_P/CD_L ratios compared to the non-TNBC tissue (BT-474) (Figure S3). These findings were further supported by the quantification results of CD_P/CD_L ratios (Fig. 2(C)).

Despite the obvious difference of CD_P/CD_L ratios in these tissues, it is important to note that these ratios alone may not accurately reflect the actual rates of de novo lipogenesis and protein synthesis. This is because these values are influenced by both the synthesis and degradation processes of biomolecules. To gain insights into the synthesis of lipids and proteins, we further investigated their turnover rates by quantifying their signals in the C-D and C-H channels, respectively.

To investigate lipogenesis, we employed a proteinase K treatment to remove proteins from the tissue samples. Subsequently, we acquired DO-SRS images of newly-synthesized lipids (CD_L) and total lipids (CH_L) at 2130 and 2850 cm^{-1}, respectively (Fig. 3(A, B)). By generating ratiometric images of CD_L/CH_L, we observed significantly higher lipid turnover in MDA-MB-231 tissue (subtype MSL) compared to other subtypes (Fig. 3(C)). The quantification results confirmed the statistical significance of this difference, while no substantial differences were observed between other TNBC subtypes and BT-474 tissue (Fig. 3(D)). These findings indicate that lipid

Biomedical Optics EXPRESS

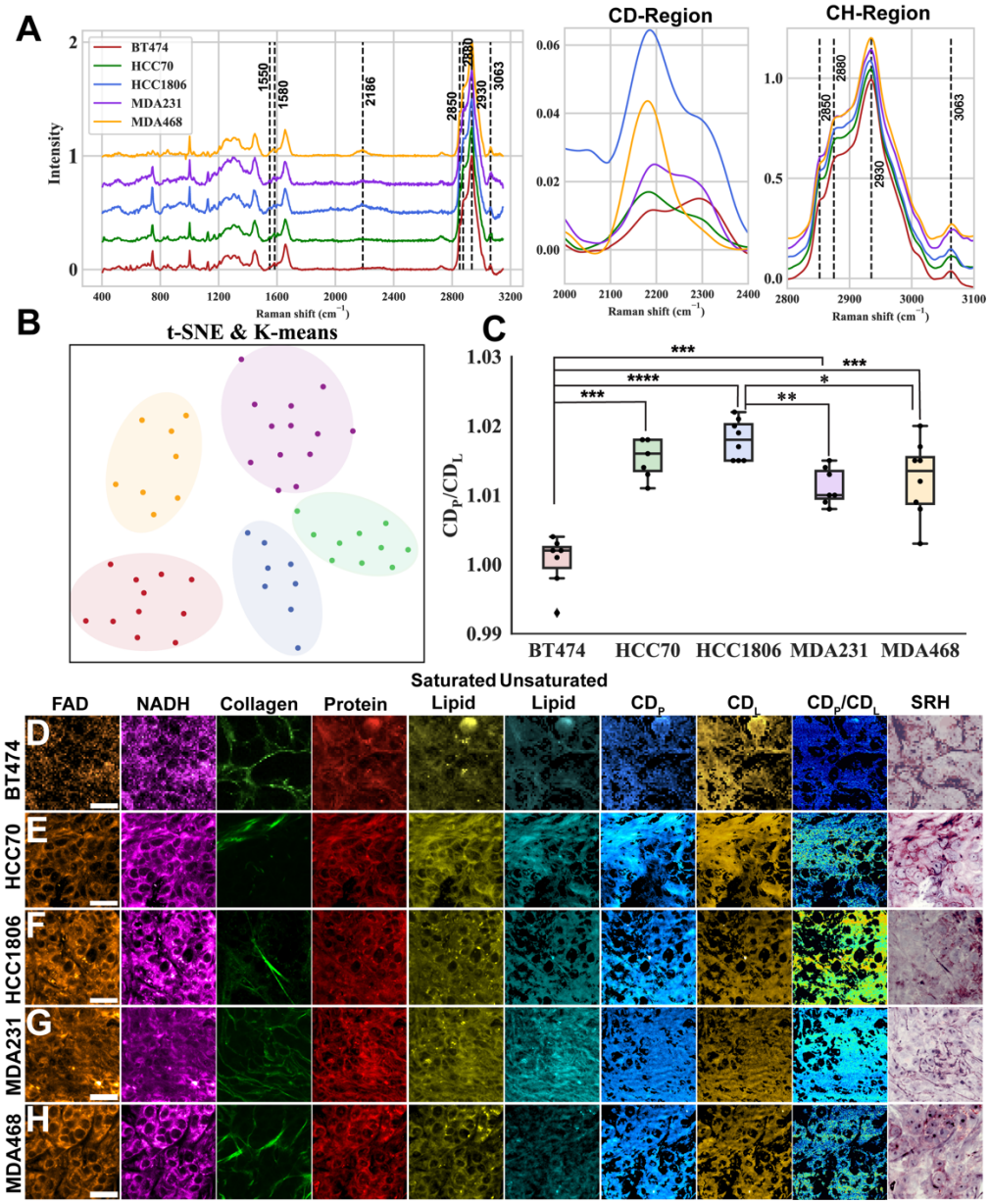

Fig. 2. Raman spectra and DO-SRS imaging of protein and lipid metabolism in TNBC tissues. **(A)** Raman spectra of TNBC tissues of different subtypes. Peaks in C-D region and C-H region are enlarged (right panel). **(B)** t-SNE-k-means clustering based on Raman spectra to differentiate TNBC subtypes. **(C)** Quantification of newly-synthesized protein relative to lipids (CD_P/CD_L). Statistical significance was determined by using one-way ANOVA test. *, $p < 0.05$; **, $p < 0.01$; ***, $p < 0.001$; ****, $p < 0.0001$. **(D-H)** Multichannel images in the same ROIs among different tumor subtypes**.** Scale bar: 20 µm.

Biomedical Optics EXPRESS

turnover could potentially serve as a biomarker for distinguishing TNBC subtype MSL from other subtypes. Additionally, we observed a greater presence of lipid droplets in TNBC subtypes compared to non-TNBC tissue (BT-474), suggesting that TNBC tumors require higher lipid levels to sustain themselves under metabolic stress (Fig. 3(A, B)).

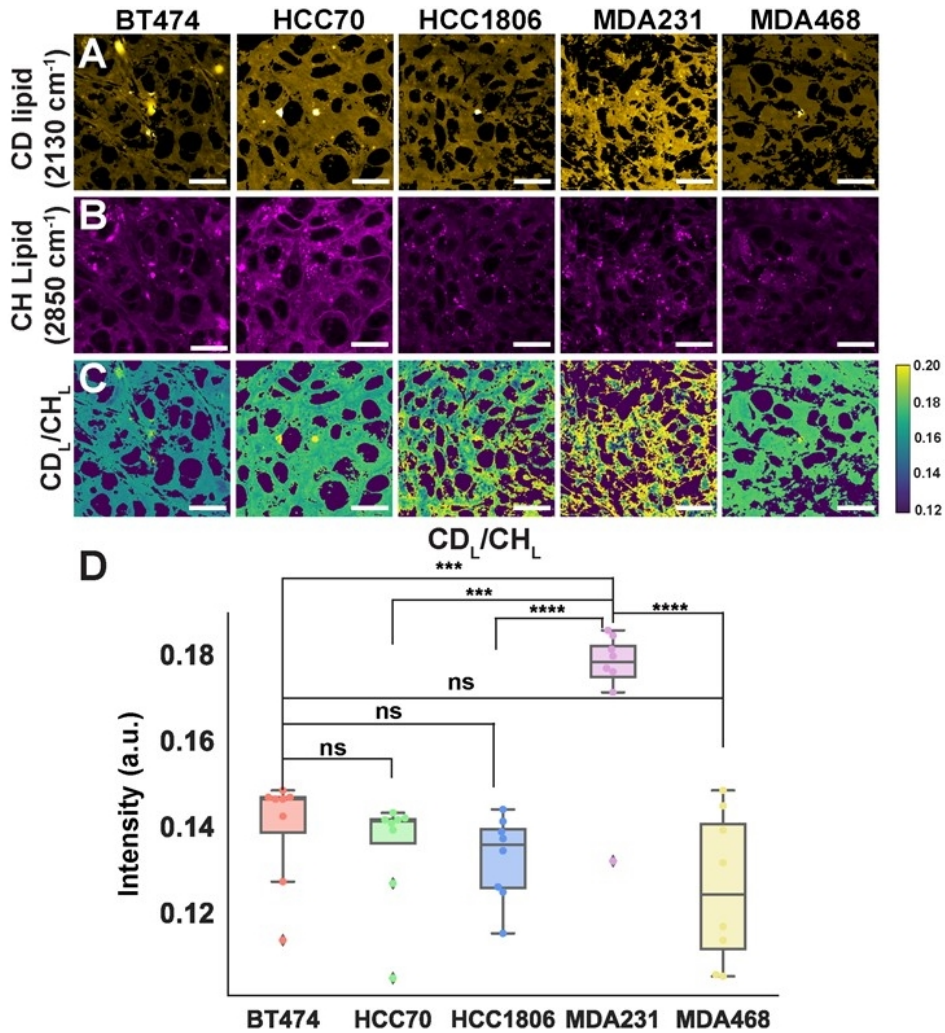

Fig. 3. DO-SRS imaging of lipid metabolic activity in TNBC subtypes of breast cancer tissues. **(A, B)** SRS images of newly synthesized and total lipid distribution in different types of tumors, respectively. These samples are treated with proteinase K, which breaks down proteins to reveal clearer lipid signal. **(C)** Ratiometric images of CD_L/CH_L in tissues. **(D)** Quantification of lipid turnover rate. There was a significantly higher lipid turnover rate in MDA-MB-231 tissue compared with other subtypes. Statistical significance was determined by using one-way ANOVA test. ***, $p < 0.001$; ****, $p < 0.0001$. Scale bar: 20 µm.

To investigate the process of de novo protein synthesis, we utilized methanol to eliminate lipids from the tissue samples. Subsequently, we obtained DO-SRS images of newly-synthesized protein (CD_P) and total protein (CH_P) at 2180 and 2930 cm^{-1}, respectively (Fig. 4(A), B). The ratiometric images clearly demonstrated considerably higher rates of protein turnover in HCC1806 (subtype BL2) and MDA-MB-231 (subtype MSL) tissues (Fig. 4(C)). Through quantification,

Biomedical Optics EXPRESS

we determined that HCC1806 tissue exhibited the highest protein turnover rate, followed by MDA-MB-231 tissue, while the non-TNBC BT-474 tissue displayed the lowest rate (Fig. 4(D)). These findings suggest that protein turnover rate can serve as a distinguishing factor for HCC1806 and MDA-MB-231 compared to other TNBC subtypes. Furthermore, it can also be utilized to differentiate HCC1806 from HCC70, despite them both belonging to the same BL2 subtype.

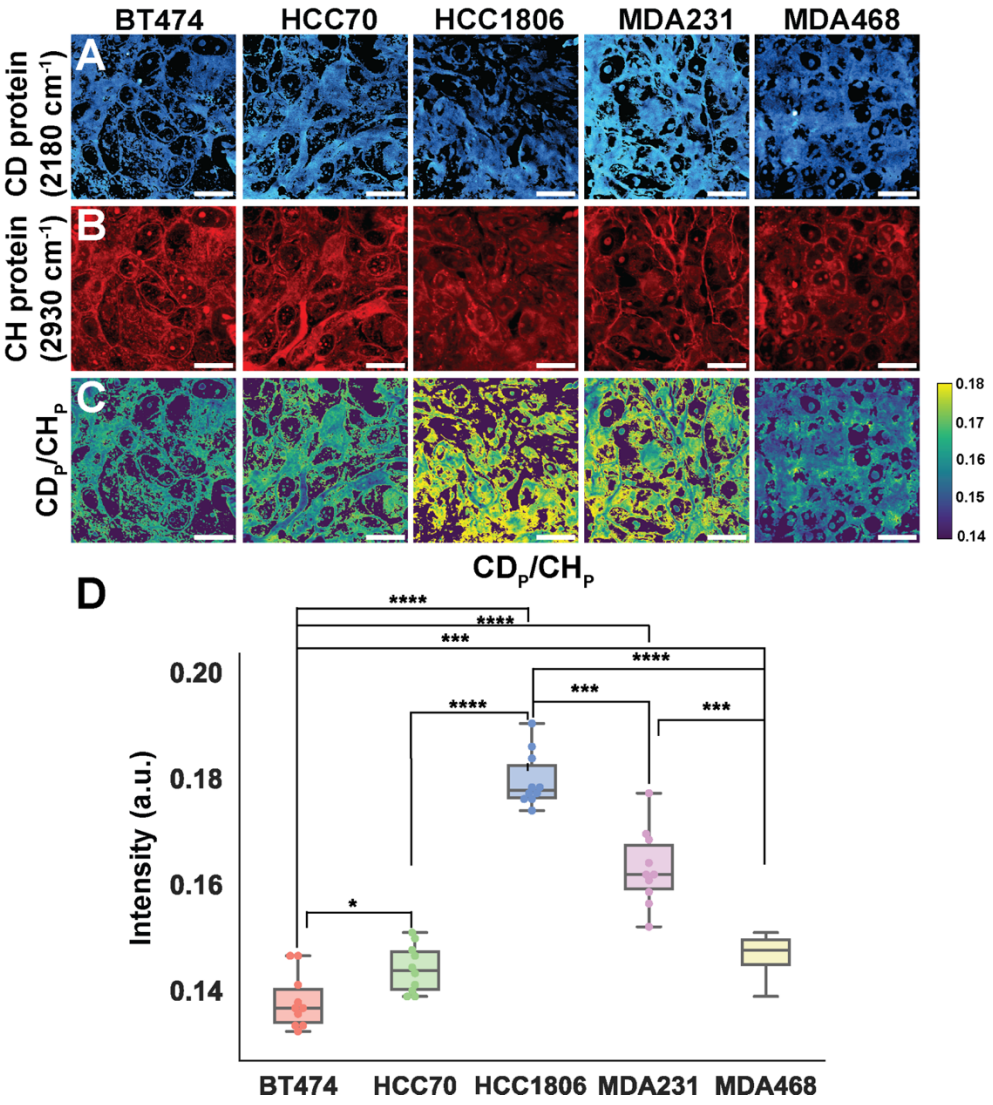

Fig. 4. DO-SRS imaging of protein metabolic activity in tissues. **(A, B)** SRS images illustrated the newly synthesized and total protein distribution in TNBC tissues, respectively. These samples were treated with methanol, which eliminated lipids to reveal clearer protein signal. **(C)** Ratiometric images of CD_P/CH_P. **(D)** Quantification of protein turnover rate. HCC1806 tissue had significantly high protein turnover and non-TNBC tissue (BT-474) had the lowest. Statistical significance was determined by using one-way ANOVA test. *, $p < 0.05$; ***, $p < 0.001$; ****, $p < 0.0001$. Scale bar: 20 µm.

Biomedical Optics EXPRESS

3.3. SRS imaging mapping cytochrome c, aromatic amino acids and unsaturated lipids

In addition to investigating lipid and protein metabolism, we further explored the characterization of other important biomolecules within the tumors. This included the analysis of cytochrome c, aromatic amino acids (AAA), and unsaturated lipids, utilizing SRS microscopy in the fingerprint region (700-1700cm^{-1}) and C-H stretching region (2800-3150 cm^{-1}), respectively.

Cytochrome c, a protein involved in electron transport within the mitochondrial intermembrane space, holds key importance in regulating cellular energy metabolism and apoptosis [27,28]. In breast tumors, there is a notable increase in the levels of cytochrome c, which is associated with tumor grade and aggressiveness [29]. Consequently, cytochrome c emerges as a potential diagnostic marker for cancer and a significant target for anticancer therapeutics [30]. Furthermore, the redox state of cytochromes within the mitochondria has been implicated in treatment resistance and unfavorable prognosis in cancer cases [30].

To investigate the spatial distribution of cytochrome c in TNBC and non-TNBC tissues, we utilized label-free SRS imaging. Prior to imaging, we treated the tissues with methanol to remove lipids. SRS images for cytochrome c were acquired at 1580 cm^{-1} and compared with images of protein obtained at 2930 cm^{-1} (Fig. 5(A), B). The ratiometric images of cytochrome c to protein (1580 cm^{-1}/2930 cm^{-1}) clearly demonstrated higher levels of cytochrome c in HCC1806 and MDA-MB-231 tissues, while HCC70 tissues displayed the lowest content (Fig. 5(D), F). These findings suggest a potential association between cytochrome c and tumor grade. However, it is worth noting that non-TNBC tissues (BT-474) also exhibited significantly higher cytochrome c content compared to HCC70 and MDA-MB-468 tissues.

We then investigated the changes in aromatic amino acids (AAA) within these tissue samples. AAA, including phenylalanine, tyrosine, and tryptophan, play vital roles in stabilizing protein structure and facilitating their proper functionality [31]. Additionally, AAA serve as precursors for various metabolites. Elevated levels of AAA have been observed in breast cancer tissue, supporting the notion that metabolic abnormalities precede morphological alterations in malignant tissue [31]. Following the removal of lipid signals through methanol treatment, we acquired AAA images at 3063 cm^{-1} and with total protein images obtained at 2930 cm^{-1} (Fig. 5(C), E). Notably, the content of AAA was significantly lower in non-TNBC BT-474 tissue compared to all TNBC tissues, with the lowest levels detected in HCC70 (BL2) tissue among the TNBC samples and the highest levels observed in HCC1806 tissue (Fig. 5 G).

Finally, we examined the abundance and spatial distribution of unsaturated lipids within the tissue samples. Unsaturated lipids serve essential functions in the body, including energy supply and the maintenance of cellular membrane fluidity [32]. Additionally, these lipids have been shown to inhibit breast cancer proliferation and differentiation, potentially improving disease prognosis [33,34]. Using proteinase K-treated samples to eliminate proteins, we captured SRS images of unsaturated lipids at 3011 cm^{-1} and compared them with images of saturated lipids obtained at 2880 cm^{-1} (Fig. 6(A)-(C)). Ratiometric analysis revealed significantly stronger unsaturated lipid signals in BT-474 tissues compared to any other TNBC tissues (Fig. 6(D)). Quantitative analysis confirmed the statistical significance of this difference, with MDA-MB-468 tissues exhibiting the lowest ratio of unsaturated lipids to saturated lipids among all TNBC tissues (Fig. 6(E)). The higher level of unsaturated lipids in BT-474 tissues may indicate a restricted growth and differentiation in non-TNBC cells relative to TNBCs, thereby suggesting the comparatively lower aggressiveness of BT-474 compared to TNBC tissues [32]. Consequently, a low content of unsaturated lipids could serve as a potential biomarker for distinguishing TNBC tissues from non-TNBC tissues.

3.4. Two-photon fluorescence imaging detecting optical redox ratio

Breast tissues contain various autofluorescence (AF) molecules, including NADH, FAD, and elastic collagen fibers [32,35]. NADH and FAD play crucial roles as electron donors and acceptors

Biomedical Optics EXPRESS

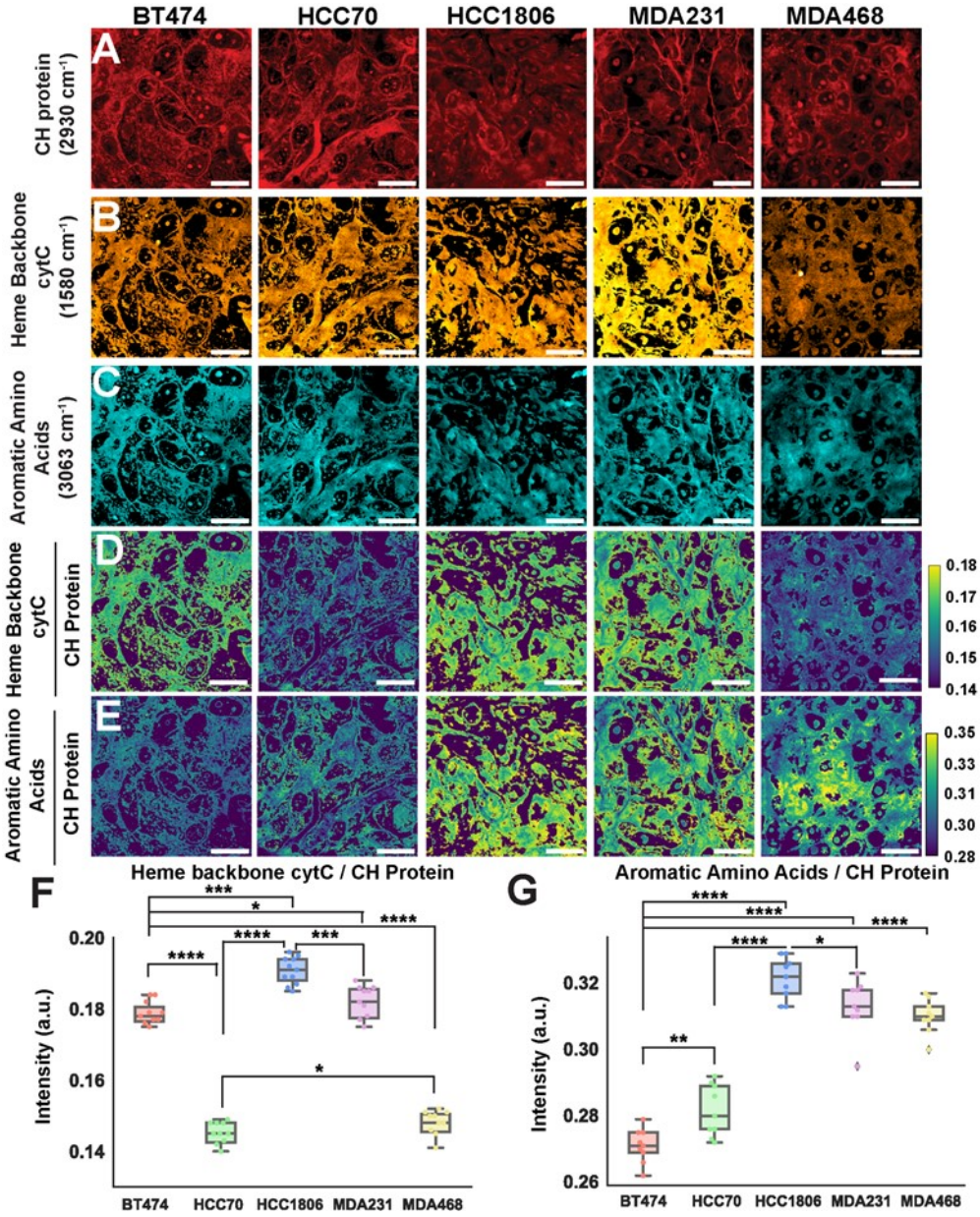

Fig. 5. Label-free SRS imaging of cytochrome c and aromatic amino acid in TNBC tissues. **(A-C)** Multichannel label-free SRS images of protein, cytochrome c and AAA in different TNBC tissues. **(D, E)** Ratiometric images displayed the relative distributions of cytochrome c and AAA to the total protein in tissues, respectively. **(F, G)** Quantitative results of ratiometric images showed significantly higher cytochrome c and AAA in HCC1806 and MDAMB-231 tissues. Statistical significance was determined by using one-way ANOVA test. *, $p < 0.05$; **, $p < 0.01$; ***, $p < 0.001$; ****, $p < 0.0001$. Scale bar: 20 µm.

Biomedical Optics EXPRESS

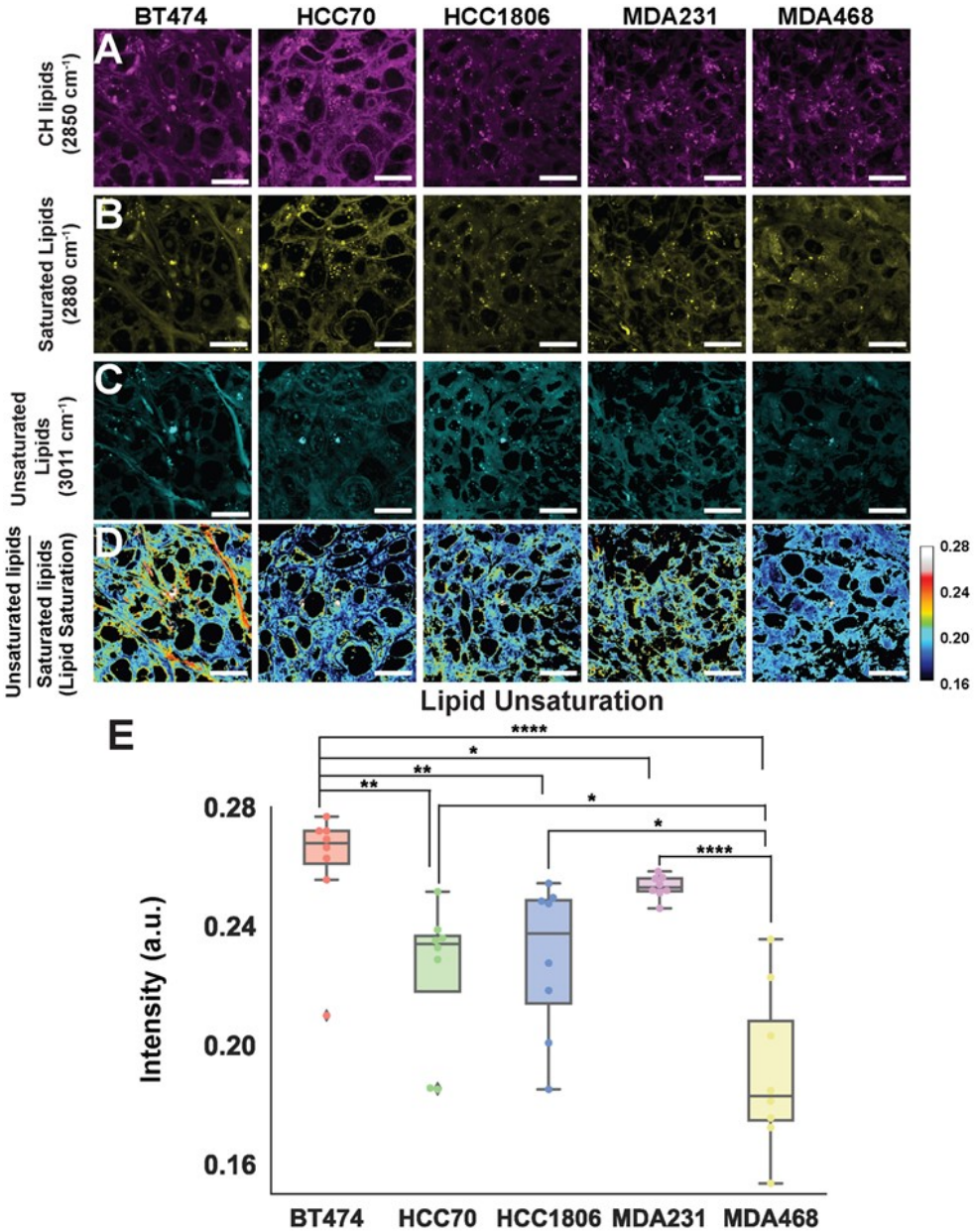

Fig. 6. Label-free SRS imaging of unsaturated lipid in tissues. **(A-C)** Label-free SRS images of total lipid, saturated lipid and unsaturated lipid in tissues. **(D)** Ratiometric images of unsaturated lipids to saturated lipids. Scale bar: 20 µm. **(E)** Quantification of unsaturated lipid in different tissues. Statistical significance was determined by using one-way ANOVA test. *, $p < 0.05$; **, $p < 0.01$; ****, $p < 0.0001$.

Biomedical Optics EXPRESS

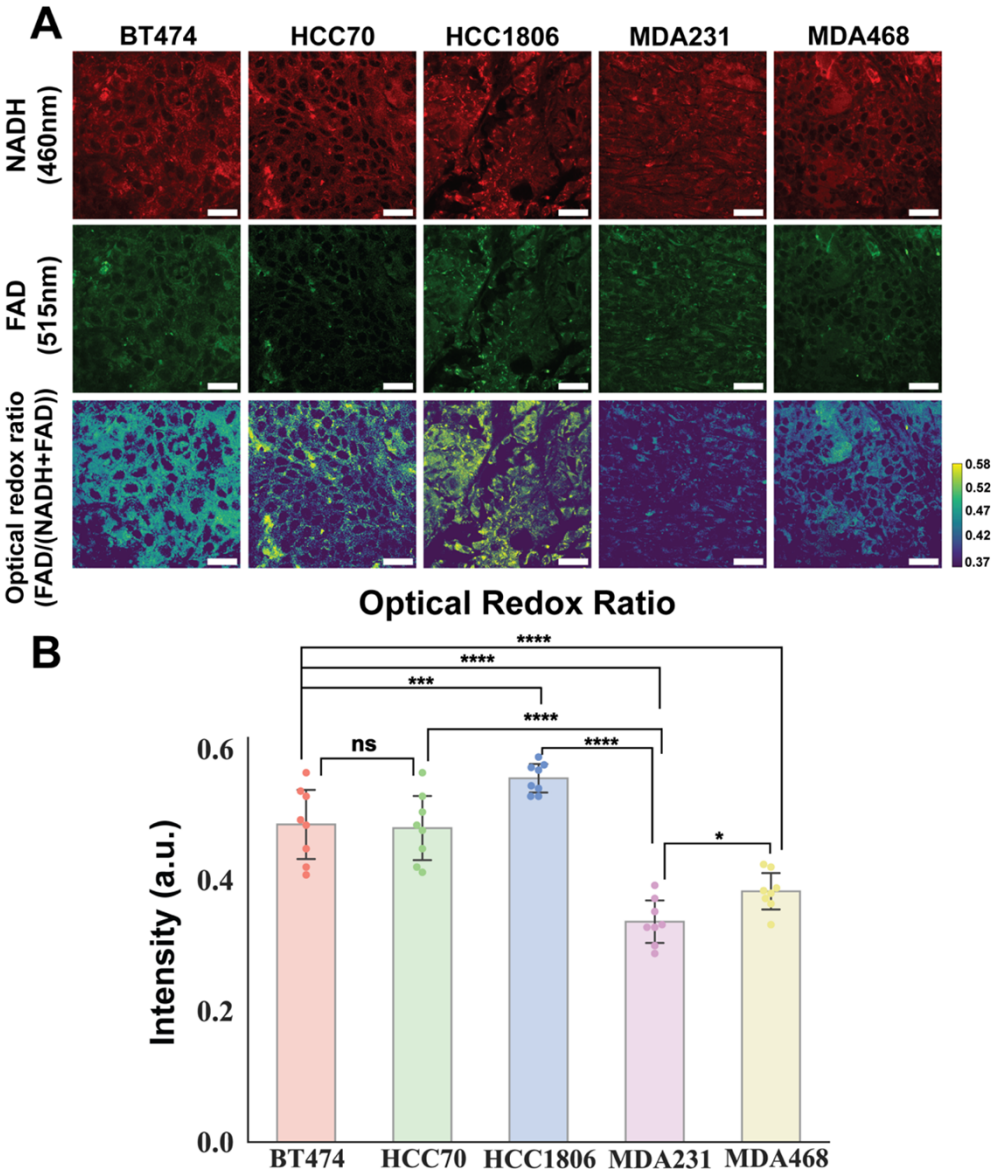

Fig. 7. Two-photon fluorescence (TPF) imaging of FAD and NADH in tissues. **(A)** TPF images of NADH, FAD, and optical redox ratio images in tissues. Ratiometric images of FAD over NADH + FAD showed different distributions of the redox ratio in BT-474 and TNBC subtypes. Scale bar 100 µm. **(B)** Quantification of optical redox ratio. In MDA-MB-231 tissues, the optical redox ratio was significantly lower than in all other tissues. Statistical significance was determined by using one-way ANOVA test. *, $p < 0.05$; ***, $p < 0.001$; ****, $p < 0.0001$.

in cellular metabolism [36]. The optical redox ratio, defined as the intensity ratio of FAD to NADH + FAD, reflects the level of cellular metabolism and the activity of mitochondrial electron transfer [7,36–38]. In this study, we utilized TPF microscopy to visualize NADH and FAD in the tissues. By analyzing ratiometric images of FAD to NADH + FAD, we obtained insights into the

Biomedical Optics EXPRESS

distribution of optical redox ratios (Fig. 7(A)). Notably, the redox ratio observed in non-TNBC BT-474 tissues exhibited significant differences compared to all TNBC tissues, except for HCC70 (Fig. 7(B)). Moreover, the redox ratio in MDA-MB-231 tissues was significantly lower than those in all other TNBC and non-TNBC tissues, which aligns with previous findings indicating weaker FAD autofluorescence in MDA-MB-231 compared to normal tissue types [39]. The reduced optical redox ratio indicates increased cellular metabolic activity during cancer progression and a shift towards mitochondrial oxidative metabolism in the MSL subtype (MDA-MB-231).

3.5. SHG imaging characterizing collagen fibers in TNBC tissues

Collagen fibers play a vital role in the extracellular matrix (ECM) of tissues, and their abundance is noteworthy [40]. Collagen has been recognized for its significant impact on morphogenesis and tumor progression, exerting control over cell behavior and influencing the tumor microenvironment [41,42]. The organization of collagen fibers has been associated with breast cancer prognosis, and quantitative analysis of collagen fiber orientation is crucial for characterizing abnormal tissue [21,43]. In recent years, second harmonic generation (SHG) microscopy has emerged as a powerful optical imaging technique for investigating the morphology of collagen fibers in cancer diagnosis [44–48]. Therefore, in our study, we employed SHG imaging to examine the orientation and distribution of collagen fibers at the tumor boundary and center, respectively (Figure S4A). Our findings revealed that collagen fibers in TNBC tissues exhibited less curvature compared to non-TNBC tissues, particularly near the tumor boundary. To quantify these observations, we computed average angles and anisotropy using a previously described methodology [49]. We observed significantly higher anisotropy in all TNBC tissues compared to BT-474 tissue in both regions, and the anisotropy was notably higher at the boundary compared to the center in all TNBC tissues (Figure S4B). These results indicate that TNBC tissues display more aggressive behavior and rapid progression at the tumor boundary. Among the TNBC tissues, there was no difference in anisotropy at the boundary. However, HCC1806 and MDA-MB-231 tissues exhibited substantially higher anisotropy at the center compared to other tissues.

4. Discussion

We have developed a novel multimodal bioorthogonal imaging platform that combines DO-SRS, TPF, and SHG imaging techniques, enabling direct visualization and differentiation of multiple TNBC subtypes and non-TNBC (BT-474) tissues in their native environment. This innovative platform provides quantitative assessment of lipid and protein metabolic dynamics using DO-SRS imaging, evaluation of the optical redox ratio through TPF imaging, and analysis of collagen morphology and orientation using SHG imaging coupled with anisotropy analysis. The integration of these modalities allows for the differentiation of TNBC subtypes based on distinct metabolic biomarkers (Figure S5). In comparison to conventional imaging methods like MRI and PET, our multimodal imaging platform overcomes the limitations in spatial resolution, enabling subcellular and quantitative imaging across various aspects to comprehensively characterize and distinguish TNBC subtypes and non-TNBC tissues. Recently developed computational algorithm for SRS can also provide support to improve spatial resolution [50]. By varying the types of deuterated metabolites, such as D-glucose [12], one can diverse the detectable information using SRS. The variation of metabolic signal will improve the capability of this multimodal imaging platform as a powerful biomarker for cancer subtype detection.

In this investigation, we employed t-SNE and k-means clustering techniques to classify Raman spectra of different TNBC subtypes based on their unique microenvironments. By utilizing DO-SRS imaging, we not only unveiled elevated metabolic activities in TNBC tissues compared to non-TNBC tissues but also identified the highest turnover rate of lipids in MDA-MB-231 (subtype MSL) tissue and the highest turnover rate of proteins in HCC1806 (subtype BL2) tissue. These findings suggest that lipids and protein metabolism may serve as potential biomarkers for

Biomedical Optics EXPRESS

distinguishing these specific TNBC subtypes. Interestingly, the other BL2 subtype (HCC70) tissue exhibited the lowest protein metabolism among the TNBC subtypes, which contrasts with the observations in HCC1806 [51]. This distinction in de novo protein synthesis between the two BL2 tissues offers new insights into the differentiation of HCC70 and HCC1806, warranting further investigation into the underlying mechanisms.

We observed a significant increase in cytochrome c levels not only in HCC1806 and MDA-MB-231 tissues but also in non-TNBC BT-474 tissue, suggesting that cytochrome c may not be a suitable marker for differentiating TNBC subtypes or distinguishing between TNBC and non-TNBC tissues. On the other hand, we found that the synthesis of AAA was significantly enhanced in TNBC tissues compared to non-TNBC tissues. Specifically, HCC1806 exhibited the highest level of AAA, followed by MDA-MB-231 tissue, indicating that AAA could potentially serve as a biomarker for distinguishing subtypes BL2 and MSL from other TNBC subtypes. Furthermore, the ratio of unsaturated lipids to total lipids plays a crucial role in maintaining cell membrane fluidity and can impact the extracellular matrix, potentially promoting rapid cell migration. Among all tissues, non-TNBC BT-474 tissue displayed the highest level of unsaturated lipids, while TNBC subtype BL1 (MDA-MB-468) exhibited the lowest level. Therefore, the measurement of unsaturated lipids may serve as a novel biomarker for distinguishing BL1 from other TNBC subtypes.

The optical redox ratio demonstrated significantly higher cellular metabolic activity in all TNBC tissues compared to non-TNBC tissue, with the most pronounced metabolic activity observed in HCC1806 tissue. Analysis of collagen fiber morphology revealed that TNBC tissues exhibited less curved collagen fibers compared to BT-474 tissue, both at the tumor boundary and center regions. Moreover, collagen fibers at the tumor boundary showed reduced curvature compared to the center region, suggesting a relationship between collagen fiber anisotropy and tumor progression. Among the TNBC subtypes, no substantial difference in collagen fiber curvature was observed at the tumor boundary. However, at the center of HCC1806 and MDA-MB-231 tumors, collagen fibers exhibited reduced curvature.

In summary, our multimodal imaging platform offers a robust and high-resolution tool for the identification of specific TNBC subtypes through multiple parameters. Through this approach, we discovered distinct metabolic characteristics associated with different subtypes: elevated protein and AAA metabolism, along with a high redox ratio, were indicative of TNBC subtype BL2 (HCC1806), while increased lipids turnover was a distinguishing feature of subtype MSL. Additionally, a low level of unsaturated lipids served as a marker for subtype BL1. The integration of this imaging platform has the potential to enhance TNBC prognosis and facilitate targeted therapeutic strategies. Our next move involves broadening the range of subcategories to include diverse ancestral origins and creating a data-driven repository to evaluate the feasibility of detecting early stages disease using deep learning techniques (Figure S6). We anticipate that our imaging platform will find broad applications in metabolic and cancer research, aiding in biomarker selection, drug discovery, and targeted therapy endeavors.

Funding. Hellman Foundation; National Institutes of Health (5R01NS111039, P30CA008738, R01GM149976, R21NS125395, U54CA132378, U54DK134301, U54-HL165443).

Acknowledgements. We thank Drs. Y. Li, K. Zhang, C. Metallo, J. Wu, G. Haddad, and D. Zhou for helpful discussions. We also thank Etna Judith Hernández and Verónica Hernández Tirado for language proofreading, and all other Shi Lab group members for comments. We thank the Taha Merghoub laboratory for the use of their Celigo Imager. We acknowledge support from UCSD Startup funds, NIH grants R01GM149976, U54CA132378, 5R01NS111039, R21NS125395, U54DK134301, U54-HL165443, P30 CA008738 (MSK Cancer Center Support Grant), and Hellman Fellow Award.

L.S. conceived the idea and designed the project. Z.L. conducted the imaging experiments, analyzed the data, and performed statistical analyses with the help from L.S., C.N., D.H., E.A., J.K., H.J.; E.A and S.M. did the cell doubling time, animal xenografts (including tumor doubling time), and heavy water probing experiments with the input from L.S. and J.K.; Z.L. and L.S. wrote and revised the manuscript with the input from all other authors.

Disclosures. The authors declare no conflicts of interest.

Biomedical Optics EXPRESS

Data Availability. The data generated in this study are available upon request from the corresponding author.

Supplemental document. See Supplement 1 for supporting content.

References

1. A. Goldhirsch, E. P. Winer, A. S. Coates, R. D. Gelber, M. Piccart-Gebhart, B. Thurlimann, H. J. Senn, and M. Panel, "Personalizing the treatment of women with early breast cancer: highlights of the St Gallen International Expert Consensus on the Primary Therapy of Early Breast Cancer 2013," Ann. Oncol. **24**(9), 2206–2223 (2013).
2. D. O'Reilly, M. A. Sendi, and C. M. Kelly, "Overview of recent advances in metastatic triple negative breast cancer," World J Clin Oncol **12**(3), 164–182 (2021).
3. C. Anders and L. A. Carey, "Understanding and treating triple-negative breast cancer," Oncology **22**, 1233–1239 (2008).
4. V. G. Abramson, B. D. Lehmann, T. J. Ballinger, and J. A. Pietenpol, "Subtyping of triple-negative breast cancer: Implications for therapy," Cancer **121**(1), 8–16 (2015).
5. S. A. Dass, K. L. Tan, R. Selva Rajan, N. F. Mokhtar, E. R. Mohd Adzmi, W. F. Wan Abdul Rahman, T. Tengku Din, and V. Balakrishnan, "Triple negative breast cancer: a review of present and future diagnostic modalities," Medicina **57**(1), 62 (2021).
6. B. E. Dogan and L. W. Turnbull, "Imaging of triple-negative breast cancer," Ann. Oncol. **23**(Suppl 6), vi23–vi29 (2012).
7. A. A. Fung, K. Hoang, H. Zha, D. Chen, W. Zhang, and L. Shi, "Imaging Sub-Cellular Methionine and Insulin Interplay in Triple Negative Breast Cancer Lipid Droplet Metabolism," Front. Oncol. **12**, 858017 (2022).
8. E. Bendau, J. Smith, L. Zhang, E. Ackerstaff, N. Kruchevsky, B. Wu, J. A. Koutcher, R. Alfano, and L. Shi, "Distinguishing metastatic triple-negative breast cancer from nonmetastatic breast cancer using second harmonic generation imaging and resonance Raman spectroscopy," J. Biophotonics **13**(7), e202000005 (2020).
9. K. J. I. Ember, M. A. Hoeve, S. L. McAughtrie, M. S. Bergholt, B. J. Dwyer, M. M. Stevens, K. Faulds, S. J. Forbes, and C. J. Campbell, "Raman spectroscopy and regenerative medicine: a review," NPJ Regen. Med. **2**(1), 12 (2017).
10. M. Daudon and D. Bazin, "Vibrational spectroscopies to investigate concretions and ectopic calcifications for medical diagnosis," C. R. Chim. **19**(11-12), 1416–1423 (2016).
11. K. Kong, C. J. Rowlands, S. Varma, W. Perkins, I. H. Leach, A. A. Koloydenko, H. C. Williams, and I. Notingher, "Diagnosis of tumors during tissue-conserving surgery with integrated autofluorescence and Raman scattering microscopy," Proc. Natl. Acad. Sci. U. S. A. **110**(38), 15189–15194 (2013).
12. L. Zhang, L. Shi, Y. Shen, Y. Miao, M. Wei, N. Qian, Y. Liu, and W. Min, "Spectral tracing of deuterium for imaging glucose metabolism," Nat. Biomed. Eng. **3**(5), 402–413 (2019).
13. Y. Wang, J. Xu, L. Kong, T. Liu, L. Yi, H. Wang, W. E. Huang, and C. Zheng, "Raman-deuterium isotope probing to study metabolic activities of single bacterial cells in human intestinal microbiota," Microb Biotechnol **13**(2), 572–583 (2020).
14. D. Berry, E. Mader, and T. K. Lee, *et al.*, "Tracking heavy water (D2O) incorporation for identifying and sorting active microbial cells," Proc. Natl. Acad. Sci. U. S. A. **112**(2), E194–203 (2015).
15. L. Shi, C. Zheng, Y. Shen, Z. Chen, E. S. Silveira, L. Zhang, M. Wei, C. Liu, C. de Sena-Tomas, K. Targoff, and W. Min, "Optical imaging of metabolic dynamics in animals," Nat. Commun. **9**(1), 2995 (2018).
16. Y. Li, P. Bagheri, P. Chang, A. Zeng, J. Hao, A. Fung, J. Y. Wu, and L. Shi, "Direct Imaging of Lipid Metabolic Changes in Drosophila Ovary During Aging Using DO-SRS Microscopy," Frontiers in Aging **2**, 819903 (2022).
17. Y. Li, W. Zhang, A. A. Fung, and L. Shi, "DO-SRS imaging of diet regulated metabolic activities in Drosophila during aging processes," Aging Cell **21**(4), e13586 (2022).
18. Y. Li, P. Chang, S. Sankaran, H. Jang, Y. Nie, A. Zeng, S. Hussain, J. Y. Wu, X. Chen, and L. Shi, "Bioorthogonal Stimulated Raman Scattering Imaging Uncovers Lipid Metabolic Dynamics in Drosophila Brain During Aging," GEN Biotechnology **2**(3), 247–261 (2023).
19. P. Bagheri, K. Hoang, C. Y. Kuo, H. Trivedi, H. Jang, and L. Shi, "Bioorthogonal Chemical Imaging of Cell Metabolism Regulated by Aromatic Amino Acids," J Vis Exp **195**, 65121 (2023).
20. A. Ghoneum, A. Y. Abdulfattah, B. O. Warren, J. Shu, and N. Said, "Redox Homeostasis and Metabolism in Cancer: A Complex Mechanism and Potential Targeted Therapeutics," Int J Mol Sci **21**(9), 3100 (2020).
21. H. Li, K. Bera, P. Toro, P. Fu, Z. Zhang, C. Lu, M. Feldman, S. Ganesan, L. J. Goldstein, N. E. Davidson, A. Glasgow, A. Harbhajanka, H. Gilmore, and A. Madabhushi, "Collagen fiber orientation disorder from H&E images is prognostic for early stage breast cancer: clinical trial validation," NPJ Breast Cancer **7**, 104 (2021).
22. Y. Zhan, G. J. Counelis, and D. M. O'Rourke, "The protein tyrosine phosphatase SHP-2 is required for EGFRvIII oncogenic transformation in human glioblastoma cells," Exp Cell Res **315**(14), 2343–2357 (2009).
23. H. N. Burr, F. R. Wolf, and N. S. Lipman, "Corynebacterium bovis: epizootiologic features and environmental contamination in an enzootically infected rodent room," J Am Assoc Lab Anim Sci **51**, 189–198 (2012).
24. M. Bazin, N. K. Purohit, and G. M. Shah, "Comprehensive measurement of UVB-induced non-melanoma skin cancer burden in mice using photographic images as a substitute for the caliper method," PLoS One **12**(2), e0171875 (2017).
25. D. Lazaro-Pacheco, A. M. Shaaban, S. Rehman, and I. Rehman, "Raman spectroscopy of breast cancer," Appl. Spectrosc. Rev. **55**(6), 439–475 (2020).
26. L. H. Van der Maaten, "Visualizing data using t-SNE," J. Mach. Learn. Res **9**, 2579–2625 (2008).

Biomedical Optics EXPRESS

27. H. Abramczyk, J. M. Surmacki, and B. Brozek-Pluska, "Redox state changes of mitochondrial cytochromes in brain and breast cancers by Raman spectroscopy and imaging," J. Mol. Struct. **1252**, 132134 (2022).
28. H. Abramczyk, B. Brozek-Pluska, M. Kopec, J. Surmacki, M. Blaszczyk, and M. Radek, "Redox Imbalance and Biochemical Changes in Cancer by Probing Redox-Sensitive Mitochondrial Cytochromes in Label-Free Visible Resonance Raman Imaging," Cancers **13**(5), 960 (2021).
29. X. Jiang and X. Wang, "Cytochrome C-mediated apoptosis," Annu. Rev. Biochem. **73**(1), 87–106 (2004).
30. L. J. Delinois, O. De Leon-Velez, and A. Vazquez-Medina, *et al.*, "Cytochrome c: Using Biological Insight toward Engineering an Optimized Anticancer Biodrug," Inorganics **9**(11), 83 (2021).
31. S. Contorno, R. E. Darienzo, and R. Tannenbaum, "Evaluation of aromatic amino acids as potential biomarkers in breast cancer by Raman spectroscopy analysis," Sci. Rep. **11**(1), 1698 (2021).
32. H. Zhang, L. Zhou, W. Shi, N. Song, K. Yu, and Y. Gu, "A mechanism underlying the effects of polyunsaturated fatty acids on breast cancer," Int J Mol Med **30**(3), 487–494 (2012).
33. S. T. Ganguly, "Application of unsaturated fatty acids in diseases prevention: A review," The Pharma Innovation J. **10**, 664–671 (2021).
34. H. Luo, C. Y. Chen, X. Li, X. Zhang, C. W. Su, Y. Liu, T. Cao, L. Hao, M. Wang, and J. X. Kang, "Increased lipogenesis is critical for self-renewal and growth of breast cancer stem cells: Impact of omega-3 fatty acids," Stem Cells **39**(12), 1660–1670 (2021).
35. S. Huang, A. A. Heikal, and W. W Webb, "Two-photon fluorescence spectroscopy and microscopy of NAD(P)H and flavoprotein," Biophys. J. **82**(5), 2811–2825 (2002).
36. S. Chakraborty, F. S. Nian, J. W. Tsai, A. Karmenyan, and A. Chiou, "Quantification of the Metabolic State in Cell-Model of Parkinson's Disease by Fluorescence Lifetime Imaging Microscopy," Sci. Rep. **6**(1), 19145 (2016).
37. N. D. Kirkpatrick, M. A. Brewer, and U. Utzinger, "Endogenous optical biomarkers of ovarian cancer evaluated with multiphoton microscopy," Cancer Epidemiol Biomarkers Prev **16**(10), 2048–2057 (2007).
38. B. G. Wang, K. Konig, and K. J. Halbhuber, "Two-photon microscopy of deep intravital tissues and its merits in clinical research," J Microsc **238**(1), 1–20 (2010).
39. S. Wu, Y. Huang, Q. Tang, Z. Li, H. Horng, J. Li, Z. Wu, Y. Chen, and H. Li, "Quantitative evaluation of redox ratio and collagen characteristics during breast cancer chemotherapy using two-photon intrinsic imaging," Biomed. Opt. Express **9**(3), 1375–1388 (2018).
40. D. A. Barron and D. R. Rowley, "The reactive stroma microenvironment and prostate cancer progression," Endocr Relat Cancer **19**(6), R187–R204 (2012).
41. G. Song, D. B. Darr, C. M. Santos, M. Ross, A. Valdivia, J. L. Jordan, B. R. Midkiff, S. Cohen, N. Nikolaishvili-Feinberg, C. R. Miller, T. K. Tarrant, A. B. Rogers, A. C. Dudley, C. M. Perou, and W. C. Zamboni, "Effects of tumor microenvironment heterogeneity on nanoparticle disposition and efficacy in breast cancer tumor models," Clin Cancer Res **20**(23), 6083–6095 (2014).
42. K. A. Burke, R. P. Dawes, M. K. Cheema, A. Van Hove, D. S. Benoit, S. W. Perry, and E. Brown, "Second-harmonic generation scattering directionality predicts tumor cell motility in collagen gels," J. Biomed. Opt. **20**(5), 051024 (2015).
43. A. M. Garcia, F. L. Magalhes, J. S. Soares, E. P. Junior, M. F. R. D. Lima, M. Mamede, and A. M. D. Paula, "Second harmonic generation imaging of the collagen architecture in prostate cancer tissue," Biomed. Phys. Eng. Express **4**(2), 025026 (2018).
44. A. Zoumi, A. Yeh, and B. J Tromberg, "Imaging cells and extracellular matrix in vivo by using second-harmonic generation and two-photon excited fluorescence," Proc. Natl. Acad. Sci. U. S. A. **99**(17), 11014–11019 (2002).
45. P. Campagnola, "Second harmonic generation imaging microscopy: applications to diseases diagnostics," Anal. Chem. **83**(9), 3224–3231 (2011).
46. J. Adur, V. B. Pelegati, A. A. de Thomaz, M. O. Baratti, D. B. Almeida, L. A. Andrade, F. Bottcher-Luiz, H. F. Carvalho, and C. L. Cesar, "Optical biomarkers of serous and mucinous human ovarian tumor assessed with nonlinear optics microscopies," PLoS One **7**(10), e47007 (2012).
47. R. Cicchi, N. Vogler, D. Kapsokalyvas, B. Dietzek, J. Popp, and F. S. Pavone, "From molecular structure to tissue architecture: collagen organization probed by SHG microscopy," J. Biophotonics **6**(2), 129–142 (2013).
48. X. Wu, G. Chen, J. Lu, W. Zhu, J. Qiu, J. Chen, S. Xie, S. Zhuo, and J. Yan, "Label-free detection of breast masses using multiphoton microscopy," PLoS One **8**(6), e65933 (2013).
49. A. Boudaoud, A. Burian, D. Borowska-Wykret, M. Uyttewaal, R. Wrzalik, D. Kwiatkowska, and O. Hamant, "FibrilTool, an ImageJ plug-in to quantify fibrillar structures in raw microscopy images," Nat. Protoc. **9**(2), 457–463 (2014).
50. H. Jang, Y. Li, A. A. Fung, P. Bagheri, K. Hoang, D. Skowronska-Krawczyk, X. Chen, J. Y. Wu, B. Bintu, and L. Shi, "Super-resolution SRS microscopy with A-PoD," Nat. Methods **20**(3), 448–458 (2023).
51. J. R. Espinosa Fernandez, B. L. Eckhardt, J. Lee, B. Lim, T. Pearson, R. S. Seitz, D. R. Hout, B. L. Schweitzer, T. J. Nielsen, O. R. Lawrence, Y. Wang, A. Rao, and N. T. Ueno, "Identification of triple-negative breast cancer cell lines classified under the same molecular subtype using different molecular characterization techniques: Implications for translational research," PLoS One **15**(4), e0231953 (2020).